Effect of Zr content on friction and wear behavior of Cr-Zr-N coating system

Mamoun Fellah, Linda Aissani, Mohammed Abdul Samad, Agung Purnama, Hamid Djebaili, Alex Montagne, Alain Iost, Corinne Nouveau

Effect of Zr content on friction and wear behavior of Cr-Zr-N coating system

Mamoun Fellah[1,2] | **Linda Aissani**[2,3] | **Mohammed Abdul Samad**[4] | **Agung Purnama**[5] | **Hamid Djebaili**[1] | **Alex Montagne**[6] | **Alain Iost**[6] | **Corinne Nouveau**[7]

[1]Mechanical Engineering Department, ABBES Laghrour- Khenchela University, Khenchela, Algeria

[2]Tribology, Materials Surface and Interfaces Group, Laboratory of Foundry, Annaba University, Annaba, Algeria

[3]Physics Department, ABBES Laghrour - Khenchela University, Khenchela, Algeria

[4]Mechanical Engineering Department, KFUPM, Dhahran, Saudi Arabia

[5]Centre d'Investigation Clinique (CIC) Biomatériaux de Bordeaux, Pessac, France

[6]Laboratory of Mechanics Surfaces and Processing Materials, ARTS ET METIERS ParisTech, Lille Cedex, France

[7]La.Bo.Ma.P, ENSAM, Cluny, France

Correspondence
Mamoun Fellah
Email: mamoun.fellah@yahoo.fr

Abstract

Nanostructured Cr-Zr-N thin film with different Zr content (0 to 48.8 at.%) was deposited, using an RF magnetron-sputtering technique. The structural evolution and morphological changes were performed. The tribological performances were evaluated, using a ball-on-disk type Oscillating tribometer. The tests were carried out under normal loads of 2, 4 and 6 N, respectively, with an alumina ball (Al_2O_3) as a counter face. The results showed that the crystallite size of the Cr-Zr-N system was reduced to 10.8 nm at 31.8 at.% Zr content. Morphological studies of the films showed that the roughness continuously decreased with increasing Zr content, exhibiting a value of 11.2 nm at 31.8 at.% Zr. The wear rate tends to decrease with the increasing of Zr content to reach a lowest value of 1.95 × 10-2 μm3.N.μm-1 at 31.8 at.% Zr. The wear rate and friction coefficient were lower in the samples with 31.8 at.% Zr content. The improved friction and wear resistance were attributed to the grain refinement strengthening mechanism at 31.8 at.% of Zr.

KEYWORDS

CrZrN coating, FR magnetron, friction and wear tests, physical vapor deposition, tribological behavior

1 | INTRODUCTION

Super hard coatings have been applied to increase the life-time and to improve the efficiency of machining tools for drilling, cutting, and molding.[1,2] For this, physical vapor deposition (PVD) method is mostly applied. They have been reported to increase the abrasive wear resistance [3-6] and to increase the economical benefits of coated materials.[3,7] First generation of PVD includes the deposition of ZrN, TiN, and CrN films; while more recent film deposition as such Cr-Zr-N receives increasing interests in various applications.[4,5,8]

In last two decades, the application of transition metal nitrides to protect cutting tools [9,10] has become a common practice in the manufacturing industry.[11] Transition metal nitride coatings exhibit unique properties [1,12] and they are frequently used in tribological applications.[4] The improved properties like magnetic, catalytic, chemical, mechanical and tribological make them attractive for biomedical and industrial applications.[13] Their performance is related to high young modulus, hardness and thermal stability, good wear resistance, as well as excellent corrosion and high-temperature oxidation resistance.[8,9,14,15]

Moreover, nitrides are hard and thermally stable.[14,16] Conventional binary system such as CrN and ZrN is often used to increase the lifetime [1,17] and to enhance the performance of cutting and forming tools.[11,18] CrN is one of the most important transition metal nitrides and it is valued as a protective and an anti-wear coating.[11,19] However, CrN is not suitable for particular applications such as high speed machining and applications operating in high temperature conditions due to the limitations of its binary system proprieties.[20]Various ternary coatings Cr- X- N, (X = Zr, Mo, V, W and Al) are now receiving a big attention due to

their excellent properties,[11,21,22] most prominent studies included the addition of Ti,[23] Al [24] and Zr.[21] Their properties such as high oxidation resistance and very low surface roughness as compared to the Cr-N system have been reported.[20]

The addition of Zr to CrN [20,23-27] as surface strengthening material is appealing due to their good wear and tribology performances; high hardness; high oxidation resistance; good adhesion; as well as low friction and low thermal conductivity.

A number of studies have addressed the tribological behavior of ternary Cr-Zr-N coatings.[28,29] However, those studies were limited to hardness, friction, and wear behavior of the coatings. Therefore, the objective of the present study is to investigate the correlation between the structural parameters (crystallographic orientation, lattice constant, grain size), mechanical properties (hardness, elastic modulus, and fracture toughness), and tribological behavior of Cr-Zr-N coatings as a function of Zr content.

2 | EXPERIMENTAL DETAILS

2.1 | Coating process

Cr-Zr-N films were deposited at a total working pressure (Ar + N_2) of 0.5 Pa, using radio frequency (RF) magnetron-sputtering system (NORDIKO type 3500, 13.56 MHz, 1.25 kW) with a base pressure of 3×10^{-5} Pa. Two separate target AISI 316L SS discs of diameter 6 cm each were used with a substrate to target distance of 70 mm and an angle of 45°(Cr) and −45° (Zr) from the normal. The films were deposited at 220°C for 80 minutes. The substrates were ground and polished to obtain a surface roughness (Ra) of 0.04 μm and ultrasonically cleaned for 6 minutes (each successively in trichloroethylene, methanol and acetone). Before the deposition, the substrates were etched under Ar^+ ions bombardment for 6 minutes at −700 V (350 W), 0.1 Pa, and cleaned under an Ar^+ discharge for 6 more minutes, at−500 V (250W) 0.5 Pa resulting in a 200 nm thin layer which serves as a sublayer for the deposition. The Cr-Zr-N deposition was conducted under varying Cr and Zr bias voltage (target power) from 0 V to −900 V (0 to 650 W) with N_2/Ar ratio of 0.25.

2.2 | Physical and chemical characterization

The structural proprieties, lattice parameters, and crystallite size of coating samples were determined, using the θ/2θ X-ray diffractometer (D500: SIEMENS, Munich, Germany) with Bragg–Brentano geometry, using Co K_α radiation (λ_{Co} = 0.178 nm). Film thickness, surface morphology, and fracture cross sections were examined, using a scanning electron microscope (SEM, JEOL JSM-5900LV). A Veeco-Wyko NT1100 Optical Profilometer, in PSI and VSI modes was used to evaluate the Film thickness by measuring the difference between the heights of the thin film surface and the substrate surface obtained by substrate masking during deposition or scratching/etching of thin film. The film thickness was also confirmed by measuring the film thickness of a cross section made through the film substrate using an SEM. The coating surface roughness was examined using an atomic force microscope (AFM 100. APE research). Film composition was determined by EDS, WDS detectors (EDS, WDS Oxford INCRA x-act) and X-ray photoelectron spectroscopy (XPS, Riber SIA 100); operated in fixed analyzer transmission mode, using $AlK_{\alpha 1,2,}$ 1486.7 eV excitation. The linearity of the energy scale was calibrated by the Al anode method and recorded in 0.5-eV steps for all sample. To ensure clean surfaces, samples were etched using the Ar ion gun at an accelerating voltage of 1 kV at a primary energy of 5 keV for 3 minutes. The main chamber was pumped with a Gamma Vacuum TiTan 300 TV differential ion pump (240 L/s) and titanium sublimation pump (1000 L/s), which brings the system to a lower pressure of 4×10^{-8} Pa, which increased to approximately 4×10^{-8} Pa during ion bombardment at a pass energy of 160 eV, room temperature, acceleration voltage of 5 keV, and an incidence angle relative to the surface normal equal to 60°. The beam size is <1 μm in diameter and the ion flow is about 5×10^{16} ions.cm^{-2}.s^{-1}. The spectra were calibrated by the C1s line with a binding energy of 284.5 eV. The XPS chemical composition was estimated from the area under the peaks of the core level: N1s, Cr2p, O1s and Zr3d.

2.3 | Hardness and young's modulus

Hardness and Young's modulus were evaluated from the load-penetration depth curves obtained from nano-indentation tester *(MTS XP nano-indenter)*. A continuous stiffness measurement (CSM) mode and an oscillating tip (frequency of 45 Hz and amplitude of 3 nm) were used. A diamond Berkovich indenter with tip radius of 200 nm and maximum load of 12 mN under load control of 0.05 mN/s nominal rate was used. For the diamond indenter, common values of 1150 GPa and 0.08 for Young's modulus, E_i and Poisson's ratio, v_i were used, respectively. The results were acquired from the average of five indentations.

2.4 | Adhesion strength and residual stresses

The film adhesion was evaluated by means of scratch-tests (Scratch Tester Millennium 200), which were carried out, using a Rockwell diamond indenter (diameter, radius, and conical angle of 0.2 mm, 200 μm and 120°, respectively).

The stripping speed and length were 8 mm/min and 8 mm, respectively. The scratch test min and max applied load were 5 and 60 N, respectively. Following the scratch tests, scanning electron microscope (SEM, JEOL JSM-5900LV) and EDS, WDS detectors (EDS, WDS Oxford INCA x-act) were used to evaluate and analyze the scratches.

The residual stress of the coating was evaluated, using the Newton ring method. The Newton rings were measured with an optical microscope equipped with a Michelson interferometer that allows determining the radius of curvature of the substrate R. The internal stress σ was estimated, using Stoney's equation as given in the following equation:

$$\sigma = (E.h^2)/6(1-v)Rd \quad (1)$$

where, E and ν are elastic modulus and Poisson ratio of the substrate, h and d are thickness of the substrate and the coating, respectively. The appearance of film surface and cross section was examined by field emission type scanning electron microscope (SEM)..[30]

2.5 | Tribological characterization

Friction and wear tests were carried out using a conventional ball-on-disk type Oscillating tribometer (TRIBOtester), with 5 mm stroke length, under dry condition. The tests were carried out under applied loads of 2, 4, and 6 N, and a constant sliding speed of 2 $mm.s^{-1}$, with an alumina ball (Al_2O_3:Young's modulus = 340 GPa, $HV_{0.05}$ = 2800, and density = 3.95 g/cm^3) as a counter face. The friction coefficient was determined after a sliding distance of 20 m. Before each test, the specimens and the balls were cleaned and rinsed with acetone in ultrasonic bath. After the tribological tests, the worn surfaces were analyzed by an optical and scanning electron microscope (SEM). Alumina balls and samples were weighed before and after each test. However, no significant difference in the weight was observed. Therefore, the following wear rate equation was applied to estimate the wear rate[31]:

$$W = V/F \cdot L \quad (2)$$

where V *is* the wear volume (μm^3), F *is* the normal load (N) and L is the sliding distance (μm). The wear volume was determined directly by laser profilometry. It was subsequently confirmed by the integration of the worn track profile obtained by laser and mechanical profilometry as follows:

$$V = \pi h2[R-(h/3)] + [R^2\alpha - l(R/2)\cos(\alpha)] \quad (3)$$

$$h = R(1-\cos\alpha) \quad (4)$$

$$\alpha = \arcsin(l/2R) \quad (5)$$

where l is the wear width *(μm), R* is the ball radius *(μm), h* is the trace depth *(μm);*

3 | RESULTS AND DISCUSSION

3.1 | Effect of Zr content on Cr-Zr-N morphology

The structural evolution of the Cr-Zr-N coatings with varying Zr content, were analyzed (Figure 1). The presence of CrN phase was observed through the presence of (111), (200), (311), and (220) peaks which correspond to the face center cubic (FCC) structure.[9,27,28,32] The XRD analysis (Figure 1a), shows oriented cubic CrN phase at 2θ angles of 43.49° and 51.67° which correspond to (200) and (111) planes respectively; and hexagonal Cr_2N phase at 2θ angle of 50.27° which corresponds to (111) plane.[32]

The addition of 0 to 2.6 at.% Zr slightly reduced the N/(Cr+Zr) ratios (from 0.96 to 0.94) then increased to reach a high value of 0.97 at 31.8 at.% Zr content. At 7.1 at.% Zr content (Figure 1b), the XRD spectra showed a strong (111) peak of the hexagonal Cr_2N phase at 49.70° along with a small peak of CrN (111) at 43.28°. The lattice constant of the coating (0.418 nm) is slightly greater than that of the CrN film (0.417 nm) and the bulk CrN phase *(JCPDS 001 65).* Random orientations were detected,

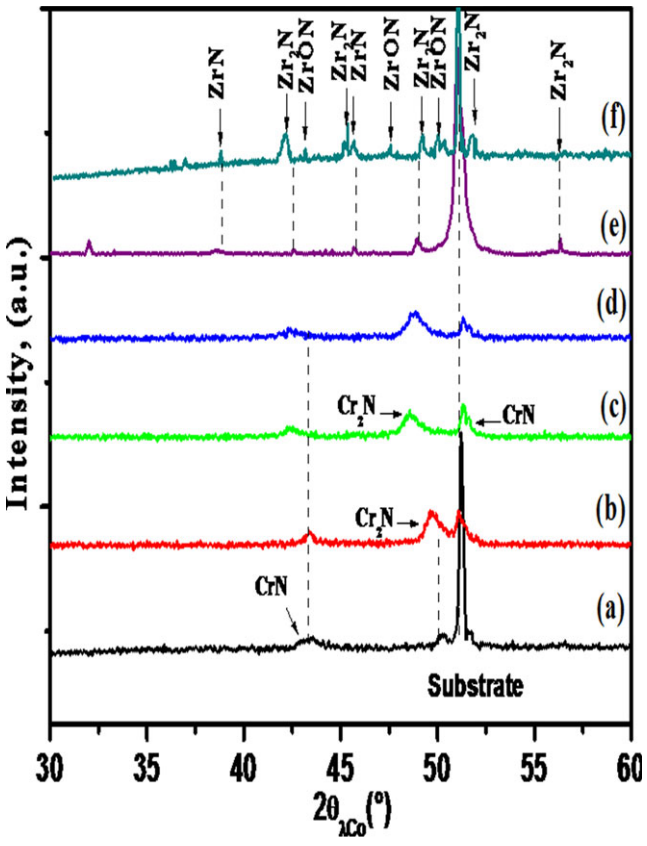

FIGURE 1 XRD patterns of Cr-Zr-N films at different concentrations of Zr: a) 0, b) 7.1, c) 26.6, d) 31.8, e) 38.6 and f) 48.8 at.% Zr [Color figure can be viewed at wileyonlinelibrary.com]

between 26.6 and 38.6 at.% of Zr content. The Cr-Zr-N system exhibited (200) and (111) orientation of ZrN and CrN, respectively, with (111) signal of Cr_2N, and (200) of Zr_2N (Figure 1c-e).

In addition, the position of the (111) CrN X-ray diffraction peak continuously shifted toward the lower (2θ) diffraction angles with increasing Zr content suggestively due to the excess of N atoms in the crystal lattice which changed the lattice constants; the presence of compressive stresses; the dense structure; or the ion bombardment energy during the deposition process.[20,30,32] On the other hand, the (111) CrN peak intensity considerably reduced with increasing Zr content.

In case of Zr-N; the coating was composed of a mixture of Zr_2N and ZrN phases with an atomic ratio (N/Zr) of 0.97. The XRD spectrum showed that the films were composed of well-crystallized ZrN (200) phase which corresponds to a high intensity peak at 45° *(JCPDS 002 0956)* and to low intensity peaks of (111) ZrN at (38.9°), (111), (200) and (121) Zr_2N peaks at 43.86, 49.05 and 56.25°, respectively, *(JCPDS 046 1204)*.[33] Moreover, minor ZrNO (444) and (751) diffraction peaks were also observed at 39.95° and 48.21° (JCPDS (00-018-1450), respectively. The stoichiometry of Cr-Zr-N films was not entirely attained due to the residual oxygen (about 2 - 3.8 at.%) located in the film from the vacuum chamber and from the residual oxygen in the sputtering gas.[32]

3.2 | Effect of Zr content on crystallite size and lattices parameters

The lattice parameter < a > of Cr-Zr-N system (Figure 2) increased with increasing Zr content from 0.417 nm at 0 at.% to 0.422 nm at 31.8 at.% Zr, corresponding to a cell volume expansion of around 3.3 at.%. The increase can be explained by the shift of diffraction patterns at small 2θ. A significant increase in the lattice parameters was observed with the Zr addition of 31.8 at.% reaching a high value of 0.448 nm. The increase of the lattice parameters can be attributed to the following: (i) Formation of the compound; (ii) the introduction to first order constraints which act on a macroscopic scale by modifying the cell parameters of the materials.[34] The crystallite size decreased with increasing of Zr content and it reached the lowest value of 14.5 nm at 31.8 at.% of Zr content, it then increased rapidly at 48.8 at.% Zr content reaching the highest value of 20 nm.

At 0 at.% Zr, the lattice parameter of 0.417 nm and the crystallite size of 18.5 nm were calculated from (200) and (111) diffraction peaks. The positive deviation of 2θ plane position and lattice parameter indicates a compressive residual stress ($\sigma_{CrN} = -1.98$ GPa, Figure 2).[30]

In case of CrZrN, the lattice parameters (Figure 2) increased steadily (0.452 nm) as the content of Zr

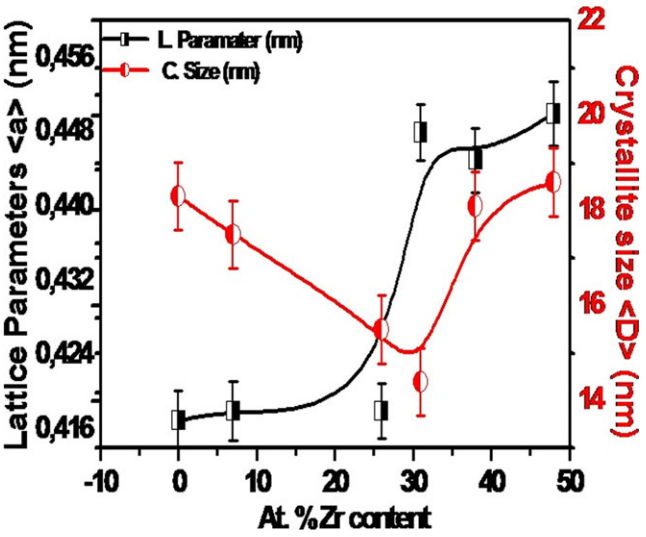

FIGURE 2 Average crystallite size and lattice parameters of Cr-Zr-N systems versus Zr content [Color figure can be viewed at wileyonlinelibrary.com]

increased. This can be attributed to the fact that, increasing Zr/Cr ratio will cause more Zr ions to occupy the sites of the Cr ions leading to the formation of a new solid solution.[20] The crystallite size, as determined from the XRD peaks, varied from 14.21 to 18.55 nm without any significant correlation with the increase of Zr/Cr ratio.

At 48.8 at.% Zr; a lattice parameter of 0.451 nm which was calculated by ZrN (111) plane was greater than that calculated for bulk ZrN phase *(JCPDS 002 0956)*. This difference can be attributed to several different effects, including the selective entrapment of interstitial nitrogen atoms and the growth of lattice defects during deposition.[32]

3.3 | Effect of Zr content on XPS analysis

Figure 3 shows the XPS spectra of CrZrN coating. In case of CrN film; the Cr ($2p_{1/2}$, $2p_{3/2}$) peaks are composed of spin–orbit doublets, with a separation of 9.6 eV; corresponding to binding energies of 574.52 eV and 583.79 eV, respectively (Figure 3a). The N1s spectrum shows a single wide peak at 397.6 eV (Figure 3b). This value indicates the CrN formations.[35,36]

For the Cr-Zr-N films; N1s peaks show the same tendency for the three coatings with the binding energies of 397.16–397.24 eV (Figure 3b-d). However, at 7.1 at.% of Zr content, CrZrN showed a lower intensity compared to the intermediates and higher content of Zr (26.6, 31.8 and 48.8 at.% Zr), which is an indication of a changed growth mode. For Cr_{2p}, XPS measurements revealed a progressive negative shift from (574.75, 584.15 eV) for 7.1 at.% and 31.8 at.% Zr down to (574.15, 584.48 eV) for 38.6 at.% Zr (Figure 3b). These results suggest the formation of Cr-Zr-N solid solution.[33,36-38]

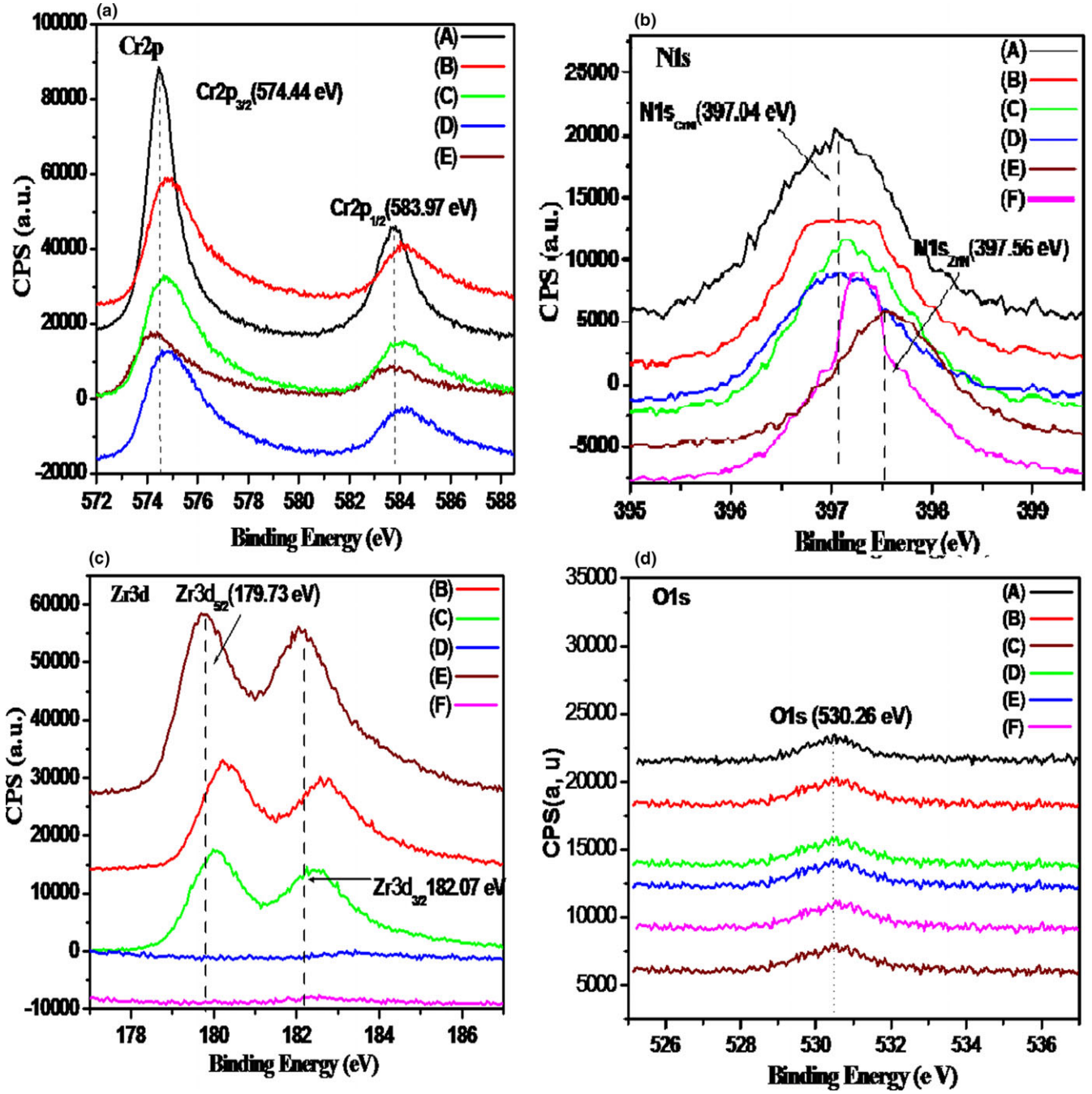

FIGURE 3 a) Cr2p, b) N1s, c) Zrd and d) O1s Spectrum of Cr-Zr- N systems versus Zr content A) 0, B) 7.1, C) 26.6, D) 31.8, E) 38.6 and F) 48.8 at.% at 2 N [Color figure can be viewed at wileyonlinelibrary.com]

TABLE 1 Chemical composition of Cr-Zr-N systems versus Zr content

	N(at.%)		Cr (at. %)		O (at. %)		Zr (at. %)		N/(Cr + Zr)	
Films	**EDS**	**XPS**	**EDS**	**XPS**	**EDS**	**XPS**	**EDS**	**XPS**	**EDS**	**XPS**
Pur CrN (0 at.% Zr)	47.8	47.8	50.0	48.9	2.2	3.3	-	-	0.96	0.97
CrZrN (7,1 at.% Zr)	47.4	47.8	39.6	43.2	2.0	2.0	7.2	7	0.94	0.95
CrZrN (26.6 at.% Zr)	47.3	47.8	18.3	22	3.6	3.6	26.8	26.6	0.94	0.98
CrZrN (31,8 at.% Zr)	47.3	47.8	19.1	18.6	2.0	2.0	31.6	31.6	0.97	0.95
CrZrN (38,6 at.% Zr)	46.7	47.6	10.9	10.5	3.1	3.8	38.6	38.6	0.94	0.96
Pure ZrN (48.8at.% Zr)	47.4	47.8	-	-	3.8	2.2	48.8	50	0.97	0.96

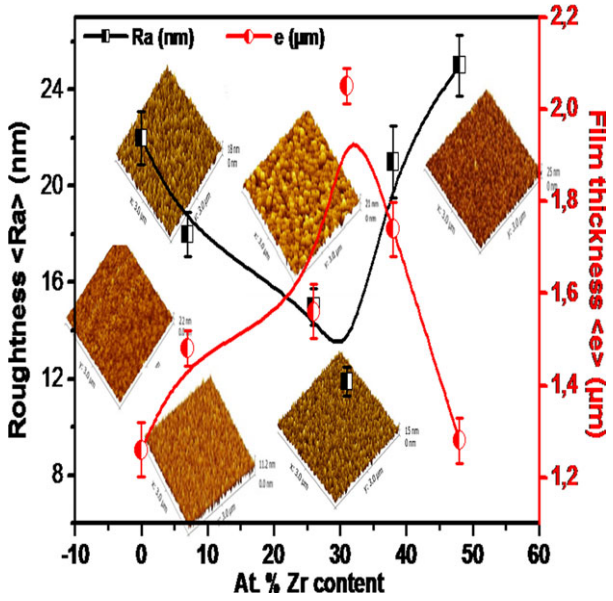

FIGURE 4 Roughness analysis, Ra (nm), surface morphologies and thickness evolution (µm) of Cr-Zr-N systems versus at.% Zr [Color figure can be viewed at wileyonlinelibrary.com]

The peaks shifted from (180.22, 182.62 eV) at 31.8 at.% of Zr to (180.03, 182.43 eV) at 48.8 at.% of Zr content, respectively, corresponding to the Zr-N band.[23,39,40] It was observed at 7.1 at.% Zr content that Zr_{3d}, and N_{1s} peaks were found to be located at (179.3 eV, 182.62 eV) and 397.3 eV, respectively. The peaks corresponding to these binding energies can be attributed to Zr-N bonding. (Figure 3d).

The atomic concentrations of Cr, Zr, N, and O on Si (100) substrates were determined by EDS and XPS analysis presented similar values. The results are listed in Table 1. From the EDS results, Cr-Zr-N films are made of stoichiometric metastable phases (CrN, ZrN). But the atomic composition derived from peak areas shows that (N/Cr+ Zr) ratio is always lower than 1. In order to understand this result, the stoichiometry of the films has been measured, using XPS. The combination of these techniques gives the stoichiometry of the films which varies from CrN to Cr2N when the Zr percentage increases from 7.1 to 38.6 at.%. A correlation between the bulk stoichiometry of the films and

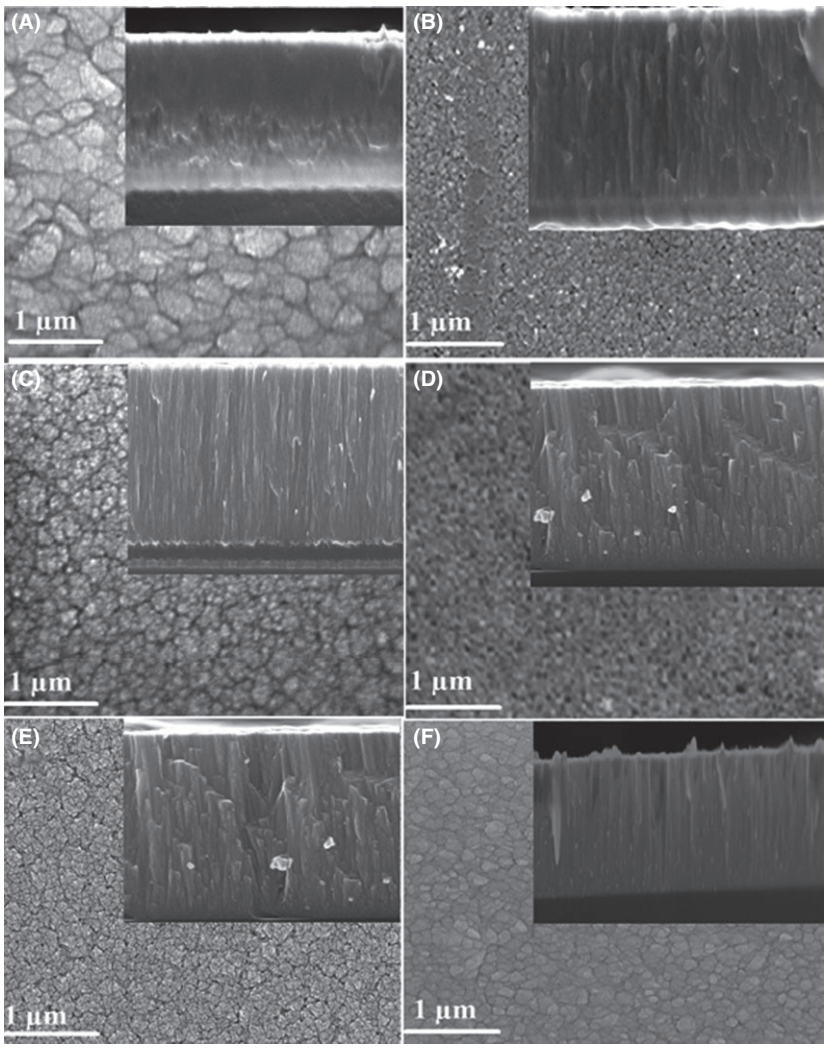

FIGURE 5 SEM morphology and cross section of Cr-Zr-N films versus Zr content: (A) 0, (B) 7.1, (C) 26.6, (D) 31.8, (E) 38.6 and (F) 48.8 at.% Zr

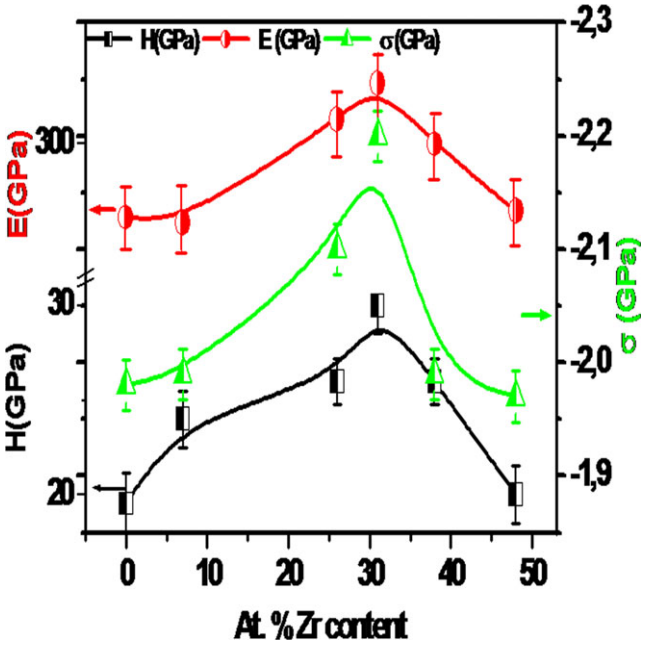

FIGURE 6 Hardness (H), Young's modulus (E) and residual stress (σ) for Cr-Zr-N films versus Zr content [Color figure can be viewed at wileyonlinelibrary.com]

the Cr2p, Zr3d, and N1s XPS peaks shapes and positions has been observed. We can also conclude that, the CrN component of the N1s peak is correlated to a Cr-N stoichiometry. The ZrN component is correlated to a Zr-N stoichiometry mixture. Otherwise, the Cr-Zr-N compounds are not yet well defined by the existence of (Cr-N, Zr-N) mixture.

3.4 | Effect of Zr content on roughness analysis

The roughness analysis and the fracture cross section of Cr-Zr-N coating is presented in Figures 4 and 5. The SEM images demonstrate that the Cr-Zr-N multilayer coatings were produced periodically. The relative dark layers correspond to the Cr layers and the gray-white are the CrN layers.

The resulting roughnesses of Cr-Zr-N coatings as a function of Zr content are displayed in Figure 4. The thickness of bilayer periods is 1.26, 1.48, 1.56, 2.05, 1.74 and 1.28 μm as a function of Zr content (0, 7.1, 26.6, 31.8, 38.6, and 48.8 at.%), respectively (Figure 4). The CrN coating shows a dense columnar structure with a roughness of 21.5 nm maybe due to a compressive stress state of the coating.[40] Additionally, this coating displays a small grain size without microdroplets or craters in the surface morphology as a result of the mutual interference of the intermediate CrN and Cr_2N phases.[23] The thickness of CrN coating was 1.26 μm, which belongs to the structure of zone II.[23,40] With an increase of Zr content from 7.1 to 31.8 at.%, the Cr-Zr-N coating showed a smooth and columnar growth, with a RMS roughness value decreasing from 15.5 to 11.2 nm (Figure 5B,C), which is related to the multicomponent coatings.[41,42] As the Zr content increases to 48.8 at.%, a mixture of round and faceted grains were found without defects (Figure 5D), indicating the existence of a random structure with the appearance of (111) Cr_2N and (002) Zr_2N peaks. However, a significant increase of roughness (21.5 nm) could be related to the film thickness; the new structure composite formation; and the competitive growth between Cr_2N and CrN.[43] The ZrN coating also showed a dense columnar structure with small grain size (Figure 5E). The ZrN coating exhibited low thickness (1.28 μm) and higher roughness (25 nm). This structure is compatible with zone II.[41,44]

3.5 | Effect of Zr content on Hardness and Young Modulus

The evolution of hardness (H), Young's modulus (E), and residual stress (σ) of Cr-Zr-N films with the addition of Zr was studied (Figure 6).The highest values were obtained at 31.8 at.% Zr (H = 30 GPa and E = 320 GPa) and the lowest values were obtained for pure ZrN and CrN (20 GPa and E = 289 GPa and H = 19.55 GPa and E = 287.91 GPa, respectively). At 38.6 at.% Zr content, the Cr-Zr-N system exhibits a slightly higher hardness value of H = 26 GPa and E = 300 GPa. It is noteworthy to point out that the average crystallite size reduction, the presence of hexagonal Cr_2N and Zr_2N phases (Figure 1) and also the compressive residual stresses σ_{CrN} = –1.98 GPa, σ_{ZrN} = –1.96 GPa could improve coating hardness and Young's modulus by grain refinement strengthening mechanism..[16,18,23,30,45,46]

The mechanical properties improvement of Cr-Zr-N coating cannot be easily explained because they are the result of complex influences of the chemical and physical properties, the growth mode, the film morphology, and the stress state.

The mechanical properties of Cr-Zr-N were improved suggestively due to the solid solution hardening which inhibits the mobility of the dislocations by the distortion of CrN lattice parameter with Zr insertion in the film.[20] Or else, it can be caused by the formation of a nanocomposite structure.[23,47] In the present study, the grain size reduction *(Hall-Petch hardening effect)* can be considered as a major factor that leads to the film densification.

The crystallite orientation of Cr-Zr-N films changed from (111) CrN preferred peak to random orientation ((111) & (002) Cr_2N, (111) & (200) ZrN and (111) Zr_2N) (Figure 1), which may have contributed to the hardness by creating a large number of grain interfaces. These interfaces could stop the dislocations sliding along the CrN planes.[48]

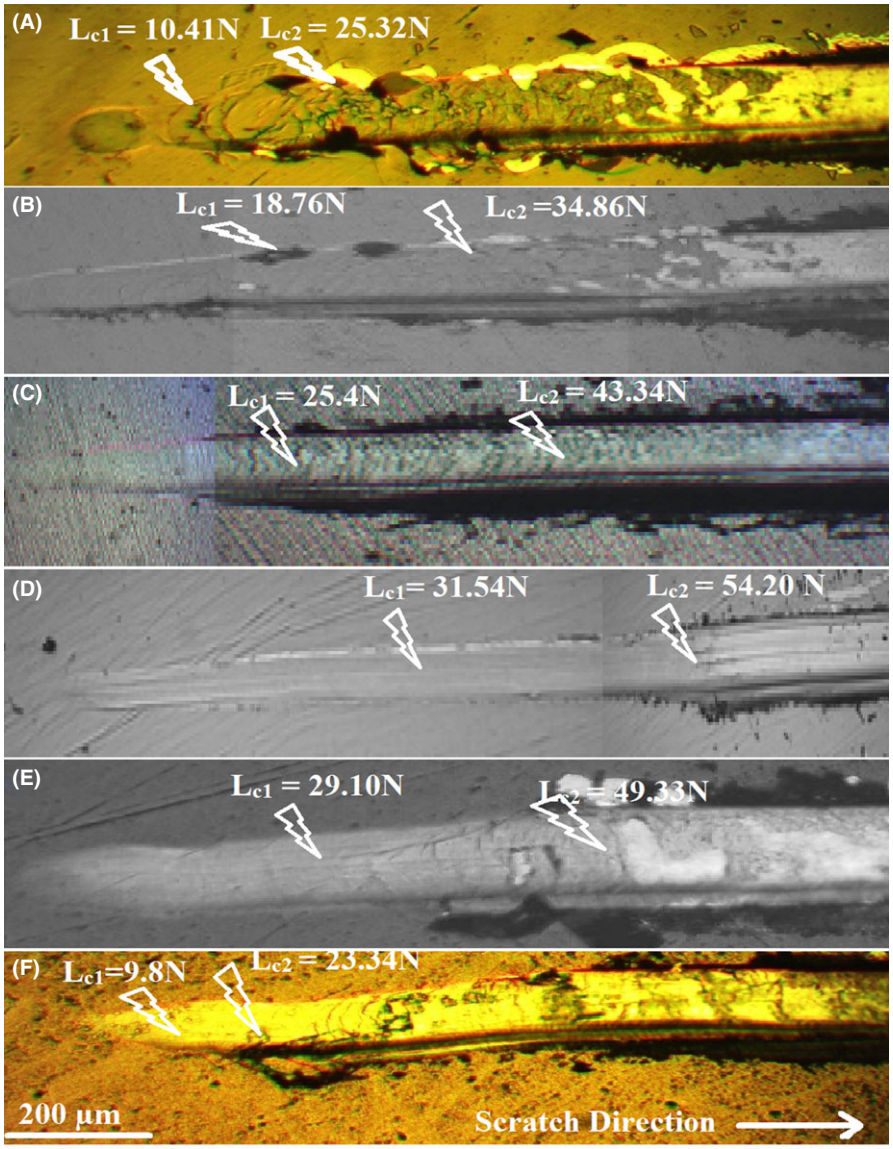

FIGURE 7 Scratch tracks micrographs versus Zr contents for: (A) 0, (B) 7.1, (C) 26.6, (D) 31.8, (E) 38.6 and (F) 48.8 at.%. Zr [Color figure can be viewed at wileyonlinelibrary.com]

On the other hand, the presence of a strong mixture of Cr–N, Zr–N phases and the presence of hexagonal Cr_2N phase may also contribute to the increase of hardness of Cr-Zr-N coatings.[49,50] According to XPS analysis, the peak shifts in Cr_{2p} binding energy suggest that the bonding character changed from the Cr-N to the Cr-Cr bonds due to the charge transfer from nitrogen to Cr atoms as a function of Zr content. This shows that Zr containing films exhibit a higher covalence level than pure CrN, which could account for the hardness increase.[18,51]

The residual stress followed the same pattern as that of hardness,[52] which showed a small increase from –1.86 GPa to –2.1 GPa at 7.1 and 31.8 at.% Zr, respectively (Figure 6). This pattern is suggestively caused by the incorporation of Zr atoms into the interstitial nitrogen sites. Alternatively, it may also have been caused by the incident of energetic particles which affected the surfaces during the film deposition.[53]

3.6 | Scratch test analysis

Figure 7 shows the SEM image and the elemental scanning of the Cr-Zr-N scratch test against Rockwell indenter as a function of Zr content. At 0 at.% Zr content, a good adhesion, wear resistance, and little damage of CrN film were observed. The cohesive and adhesive failure critical loads are in the range of $L_{c1} \approx 10.41$ and $L_{c2} \approx 25.32$ N, respectively. These lower values can be attributed to the presence of high residual stress (Figure 6) and soft AISI 316L SS substrate. At 7.1 at.% Zr content, critical load ($L_{c2} \approx 34.86$ N), smooth and adhesive wear without any sign of debris abrasion was observed (Figure 7B). Its wear rate was negligible compared to CrN coatings due to its high hardness values and low roughness.[20,35]

However, at 31.8 at.% of Zr (Figure 7D), an adhesive critical high load ($L_{c2} \approx 54.20$ N) and delamination fracture mechanism of coating was observed at the edges of

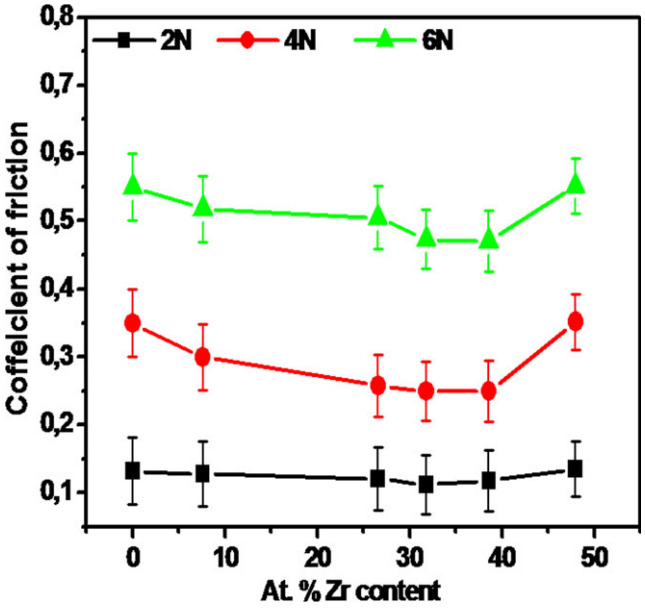

FIGURE 8 Evolution of mean friction coefficient of Cr-Zr-N systems versus Zr content [Color figure can be viewed at wileyonlinelibrary.com]

the scratch tracks. As can be seen in Figure 7E, the addition of 38.6 at.% Zr deteriorated the film adhesion due to the decrease in mechanical properties. As a result, the adhesive action is significantly lower ($L_{c2} \approx 49.33$ N) than that of 31.8 at.% Zr. Moreover, at 48.8 at.% Zr content, a significant decrease of the L_{c1} was observed ($L_{c1} \approx 9.8$ N). The ZrN film revealed a lower adhesive critical load ($L_{c2} \approx 23.34$ N). Nevertheless, a brittle failure mode was observed, this one manifested by the formation of lateral cracks and chipping at the edges and the middle of the scratch tracks (Figure 7E).

3.7 | Effect of Zr content on friction coefficient

The coefficient of friction values is reported as an average value over the complete time history (After 20 m). As illustrated in Figure 8, the coefficient of friction (COF) decreases rapidly from 0.55 to 0.128 throughout the small content of Zr (0-26.6 at.%), and subsequently decreases rapidly to reach the lowest value of 0.112 at 31.8 at.% Zr, and it slightly increases to reach a high value of 0.552 at 48.8 at.% of Zr content. However, the friction coefficient was higher for the applied load of 6 N for all tested samples. This behavior is suggestively caused by the structure in the coatings establishing a flat wear track surface by ploughing away the asperities and roughness irregularities (Figure 4).

The average friction coefficient values at 2 N was in the range of (0.112-0.135), while it varied between (0.250 and 0.352) at 4 N, and (0.470-0.552) at 6 N with varying Zr content from 0 to 48.8 at.% Zr, respectively. It was observed that the friction coefficient increases with increasing of normal load due to an increase in the true contact area.[54]

3.8 | Effect of Zr content on volume and wear rate

The wear scars, sizes, and depths of each groove were measured using a mechanical and 3D optical profilometer.

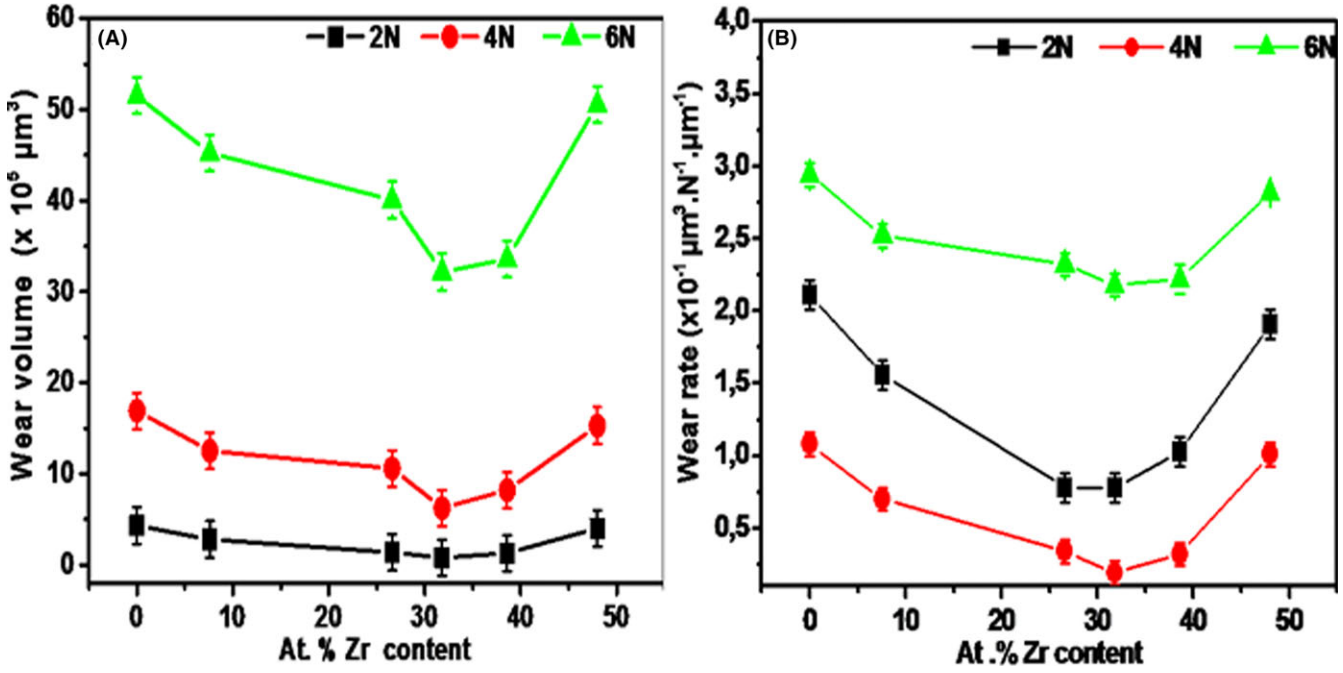

FIGURE 9 Evolution of: (A) Wear volume (x 10^5 μm^3), (B) Wear rate ($\times 10^{-1}$ $\mu m^3.N^{-1}.\mu m^{-1}$) of Cr-Zr-N systems versus Zr content [Color figure can be viewed at wileyonlinelibrary.com]

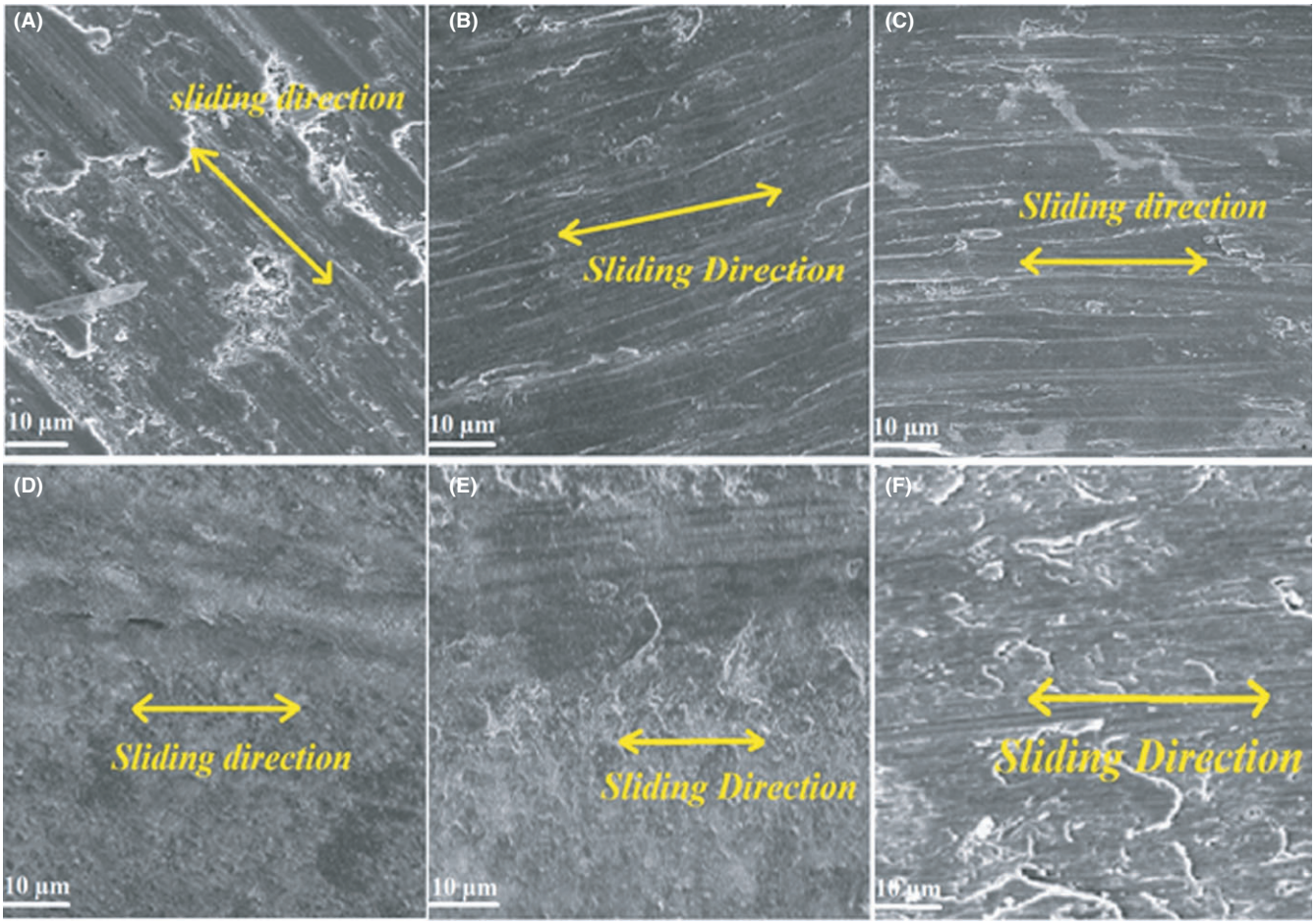

FIGURE 10 SEM images of worm surface of Cr-Zr-N system versus Zr content: (A) 0, (B) 7.1, (C) 26.6, (D) 31.8, (E) 38.6 and (F) 48.8 at.% at 2 N [Color figure can be viewed at wileyonlinelibrary.com]

A number of depth measurements were taken along the groove lengths. Wear rates were obtained from the scars profile, using optical microscope measurements.

Figure 9 illustrates the increase of wear rate with an increase in load when the concentration of Zr was fixed. When the load was fixed, the wear rate tends to decrease with increasing Zr content to reach a lowest value of 1.95×10^{-2} $\mu m^3.N.\mu m^{-1}$ at 31.8 at.% Zr. When the load equals or less than 4 N, the wear rate varied within the range of 1.95×10^{-2} to 1.08×10^{-1} $\mu m^3.N.\mu m^{-1}$; whereas at 4N, the wear rate varied within the range of 2.18×10^{-1} to 2.94×10^{-1} $\mu m^3.N^{-1}.\mu m^{-1}$, indicating that the wear was intensified. The volume and wear rate was higher at 0 and 48.8 at.% and lower at 31.8 at.% Zr content.

It was observed, that the load and Zr content play a significant role on the Cr-Zr-N wear rates. One order of magnitude between the highest and the lowest wear was calculated, confirming friction behavior and wear resistance of Cr-Zr-N coating systems do not only depend on the applied load, but also depend on their concentration of Zr. At 31.8 at.% Zr, the Cr-Zr-N system tested at 2 N exhibited lower friction, low wear rates, and better wear resistance (Figure 9). These maybe attributed to the better mechanical properties, higher hardness values, lower crystallite, and grain size.[55,56]

3.9 | SEM observations, wear debris, and subsurface structure

The wear scars morphology of CrZrN systems as a function of Zr content under applied loads of 2, 4, and 6 N, after 20 meters of dry sliding was analyzed, using scanning electron microscopy (Figures 10-13). At higher loads, a significant build up of the material on the wear track periphery and a fine particle size was observed. At 0 and 48.8 at.% Zr, an increase in the load caused wider grooves, this indicates that the abrasive wear was the dominant wear mechanism.

Figure 10A-F shows SEM micrographs of Cr-Zr-N coating worn surfaces as a function of Zr content after wear testing under a normal load of 2 N. At 0 at.% Zr, the wear tracks consisted of deeply torn grooves (Figure 10A). Moreover, a scar distinguished by a failure mechanism was

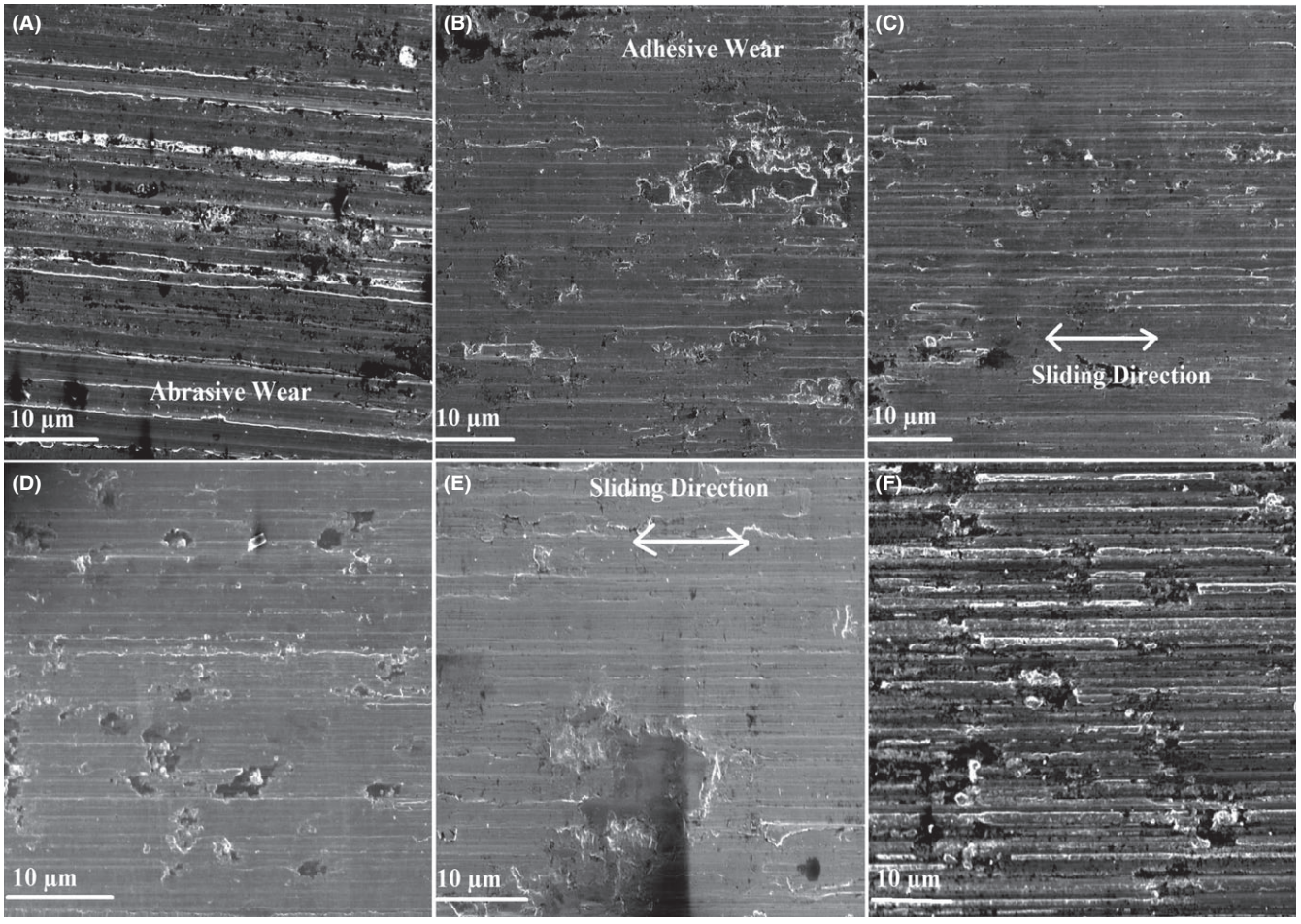

FIGURE 11 SEM images of worm surface of Cr-Zr-N system versus Zr content: (A) 0, (B) 7.1, (C) 26.6, (D) 31.8, (E) 38.6 and (F) 48.8 at.% at 4 N

observed. The observed wear mechanism was similar in all tested samples. It was initiated by a high layer detachment in the small particles form, which was an important factor to accelerate the gradual wear phenomena.These particles created the systems instability between the surfaces resulting in an increase of the temperature in the contact area, weakening the coating. In most cases, the tests were carried out until the total detachment of the coating. Nonhomogeneous wear was observed in alumina ball, forming irregular areas, which may have been caused by the movement of abrasive particles from the center to the sides of wear track. This phenomenon was observed mainly for samples tested at 6 N.

The lowest wear rate was exhibited by Cr-Zr-N coatings with 31.8 at.% Zr content as shown in Figures 8 and 9. The low coefficient of friction (0.112-0.42), as seen in Figure 9, is the most important factor that leads to low wear rates. The wear scars show a coating detachment (Figure 10C-E). However, there was no significant difference on wear morphology of Cr-Zr-N systems with three concentration of Zr (26.6, 31.8 and 38.6 at.%). In most cases, 31.8.at.% Zr gave a better wear performance than the other two concentrations of Zr (26.6 and 38.6 at.%) when 2 to 6 N load was applied. Moreover, the worn surfaces were sheltered by a smooth transfer film of compressed wear debris. However, significant marks were not observed on the surface in case of 26.6 at.% Zr as seen in Figure 10C and few marks are seen in the case of 31.8 at.% Zr as shown in Figure 10D. Some tests lasted up to 2000 cycles without any change in the areas of wear.

In the case of pure ZrN (48.8 at.% Zr), it was difficult to identify the failure and friction mechanism. The wear did not follow a traditional pattern as in the case of pure CrN (0 at.%) system. Uniform wear was not observed and it was difficult to detect visually the detachment of the coating. The worn surface morphology of the pure ZrN (48.8 at.% Zr), as shown in Figure 10F, displayed parallel grooves running along the sliding direction which are covered by black wear debris. The ZrN coating acts as a repellant to the mechanisms of failure of traditional sliding wear, resulting in small areas of wear of the coating that are isolated and irregularly shaped (Figure 10F). Noise and vibration were not apparent. The wear rates on the ball were greater than CrN film, suggesting high wear resistance of the ZrN thin film.[57] This coating, acted efficiently

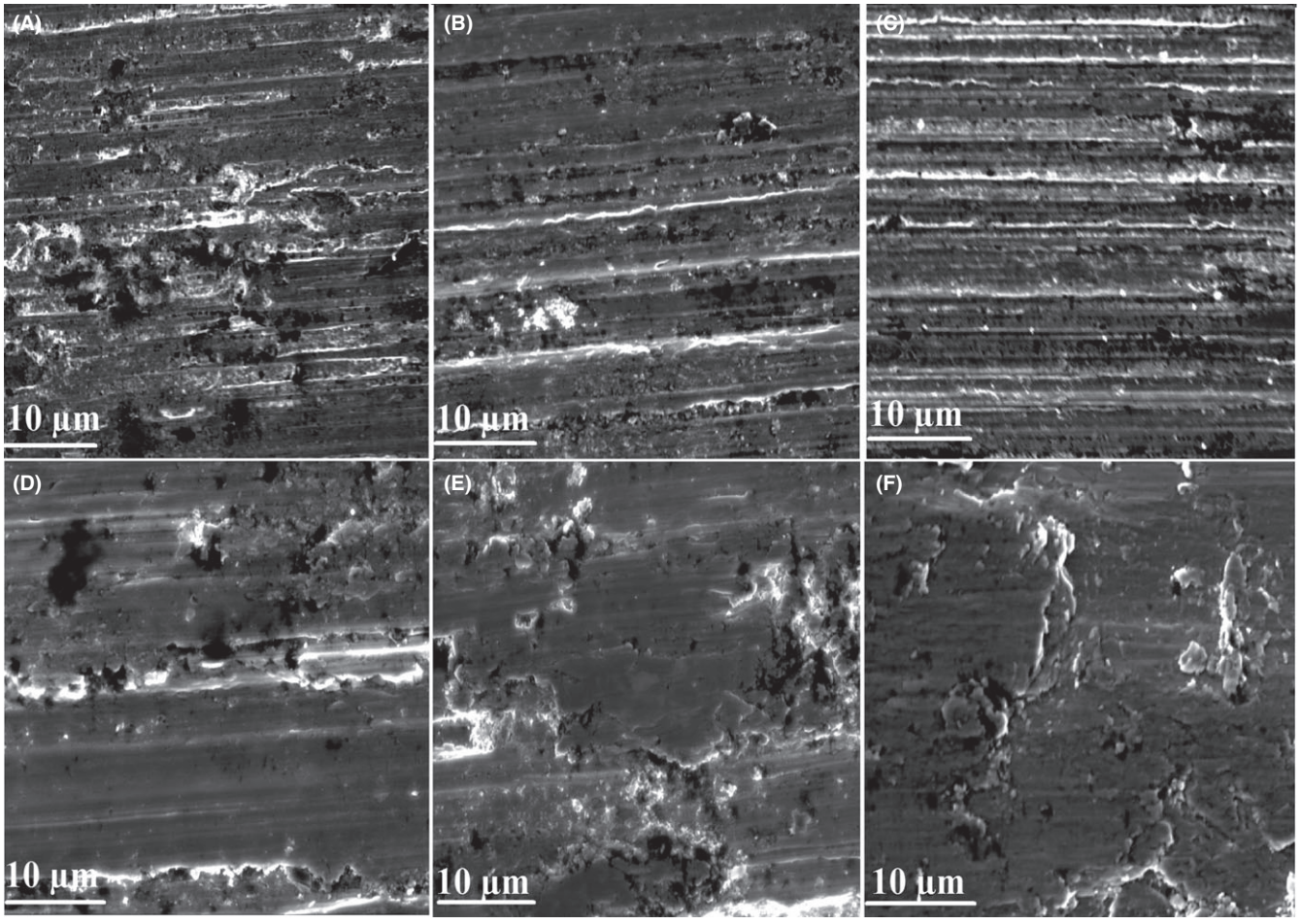

FIGURE 12 SEM images of worm surface of Cr-Zr-N system versus Zr content: (A) 0, (B) 7.1, (C) 26.6, (D) 31.8, (E) 38.6 and (F) 48.8 at.% at 6 N

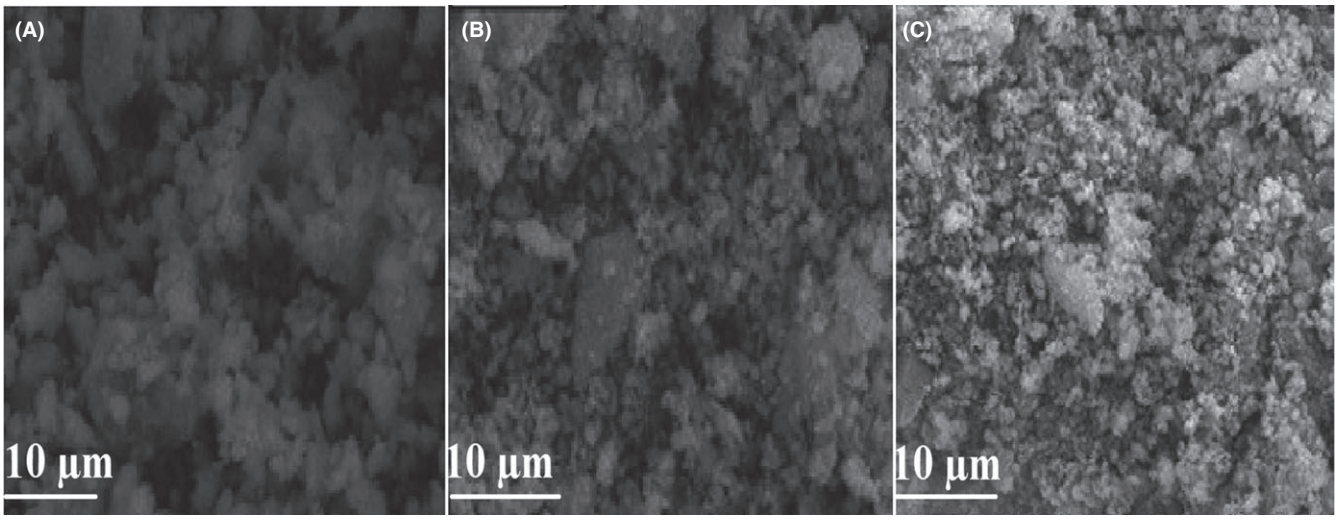

FIGURE 13 Morphology of wear debris collected after wear tests. (A) CrN, (B) Cr-ZrN and (C) ZrN

in this type of wear, showing negligible wear on the surface. This explains the frequent use of this coating in different applications, including cutting tools, guides, dies, biomedical applications, etc.[58]

Figures 11 and 12 show SEM micrographs of Cr-Zr-N coating worn surfaces with different concentrations of Zr after wear testing at 4 and 6 N normal load. For these samples, a relatively smooth wear track was observed. A

significant surface damage with deformed and smeared appearance was observed. There were small cracks on the worn surface indicating a delicate fracture. The wear track was distorted and showed a brushing off of debris on the worn surface.

With an increase in the applied load, a significant build up of the wear debris on the inner and the outer periphery (Figures 11-12) of the wear track was observed. In most of the cases, the weight loss caused by adhesive wear and lamination defect was observed. Along the wear track (Figures 10 and 12), both abrasive and adhesive wear mechanism were presented. At a lower and higher concentration of Zr (0, 7.1 and 48.8 at.%), abrasion was the major wear mechanism while at medium concentration (26.6, 31.8 and 38.6 at.% Zr) adhesion was the main wear mechanism.

The Cr-Zr-N coating microstructure can also influence the properties of materials and indirectly affect the tribological properties. The grain size and porosity of a coatings system directly influences the material properties such as thermal shock resistance and bending strength.[59] The relationship between hardness and CrZrN coatings grain size followed a Hall-Petch-type equation,[60] which involved an increasing hardness with decreasing grain size.[52,61] The CrZrN coating systems with the smallest grain size showed the lowest wear rate, as expected. Hence, the improvement in the wear performance of the CrZrN coating system with 31.8 at.% Zr can be attributed to its lower crystallite and grain size.

3.10 | Wear debris morphology

Figure 13 shows the morphology of wear debris of CrZrN coating system at 0, 31.8 and 48.8 at.% Zr content. The wear debris of pure CrN (0 at.% Zr) showed larger chip-like metallic and fine wear particles. Similar features were observed in the wear debris of pure ZrN coating (48 at.% Zr) but the particle size was finer and the chips were smaller. Some larger agglomerates of debris that were flaked off from the transfer layer could also be observed, Figure 13C. The mechanism of wear appeared to be a mixture of adhesion and oxidation (Figure 12). Wear debris particles were suggestively generated by metal transfer, delamination mechanism, or by ploughing the asperities of the counter face.

As the wear debris particles were repeatedly fragmented and oxidized, the fine particles generated became adherent to the wear surfaces and get agglomerated in some regions, particularly in the grooves.[21] The debris generated during oxidative wear may have an effect on the wear process in two different ways: (i) the oxide particles may get locked between the sliding surfaces and (ii) these particles get compacted on the sliding surface to form a protective transfer layer (Figures 10-12). Both of the friction coefficient and the wear rates decreased with increasing Zr content (Figures 8 and 9), suggestively due to lower hardness value of 0 and 48.8 at.% Zr content.

It is suggested that the beneficial role of wear debris in promoting wear resistance through formation of transfer layer is more prominent than its contribution to increase volume loss through three body wear [62] as only a few scratch marks were observed on the surface of the specimens. The presence of transfer layer was observed on the surface of all the coatings. It appeared to be more compact on the surface containing a higher amount of Zr. Hence, they showed a lower wear rate and friction in comparison to pure CrN and ZrN.

4 | CONCLUSIONS

The structural evolution and morphological changes of the nanostructured Cr-Zr-N thin film, using an RF magnetron-sputtering technique were studied. Different concentrations of Zr (0, 7.1, 26.6, 31.8, 38.6, and 48.8 at.%) were applied. The following conclusions can be drawn:

1. The deposited Cr-Zr-N coatings showed a columnar compact structure with a mixture of fcc (CrN, ZrN) and hcp (Cr_2N, Zr_2N) phases with Cr_2N (111) preferential orientation.
2. The Cr-Zr-N crystallite size decreased and the lattice parameter increased as zirconium content increased from 0 to 31 at.% with an improved roughness due to the crystallite size.
3. The highest values of hardness and Young's modulus were obtained for 31.8 at.% Zr content and the lowest values were obtained in the case of pure CrN and ZrN coatings, due to the formation of strengthening (Cr-N, Zr-N) mixture, preferred crystallite orientation and grain refinement.
4. The scratch test showed that the Cr-Zr-N adhesion was significantly improved in the case of 31.8 at.% Zr.
5. Addition of 31.8 at.% Zr resulted in a significant improvement in relative density, hardness, and wear resistance due to a reduction in the particle size.
6. At constant applied normal loads, the wear rates decreased with increasing Zr content reaching the lowest value at 31.8 at.% Zr, which was attributed to the improved mechanical properties of the coating.
7. At the same Zr content, an increase in the applied normal load increased the wear track resulting in higher wear rates.
8. The friction coefficient increased with the increase of the normal load, but decreased significantly with higher Zr content for all tested samples reaching the lowest value at 31,8 at.% of Zr.

9. At 31.8 at.% Zr content, the CrZrN system showed the lowest wear rate, while at 0 and 48.8 at.% it reached the highest wear rate. The applied load, crystallite, and grain size played an important role in controlling the wear rate. The higher wear resistance at 31.8 at.% Zr content corresponded to good mechanical and microstructural properties.
10. The predominant wear mechanisms were found to be abrasion, adhesion, and delamination for nanostructured CrZrN system.

ORCID

Mamoun Fellah http://orcid.org/0000-0003-0615-6711

REFERENCES

1. Anusha Thampi VV, Bendavid A, Subramanian B. Nanostructured TiCrN thin film by pulsed magnetron sputtering for cutting tool application. *Ceram Int*. 2016;42:9940-9948.
2. Voevodin A, Zabinski J, Muratore C. Recent advances in hard, tough, and low friction nanocomposite coatings. *Tsinghua Sci Technol*. 2005;10:665-679.
3. Divyesh PD, Kamlesh VC, Mahesh RC, et al. Study of tribological behavior for chromium based coatings deposited on conventional materials. *Procedia Technol*. 2016;23:91-97.
4. Deng J, Liu J, Zhao J, et al. Friction and wear behaviors of the PVD ZrN coated carbide in sliding wear tests and in machining processes. *Wear*. 2008;264:298-307.
5. Sanchéza JE, Sanchéza OM, Ipaza L, et al. Mechanical, tribological, and electrochemical behavior of Cr1−xAlxN coatings deposited by r.f. reactive magnetron co-sputtering method. *Appl Surf Sci*. 2010;256:2380-2387.
6. Khrais S, Lin Y. Wear mechanism and tool performance of TiAlN PVD coated inserts during machining AISI 4140 steel. *Wear*. 2007;262:64-69.
7. Donnet C, Erdemir A. Solid lubricant coatings. Recent developments and future trends. *Tribol Lett*. 2004;172:389.
8. Olaya JJ, Rodil SE, Muhl S. Comparative study of chromium nitride coatings deposited by unbalanced and balanced magnetron sputtering. *Thin Solid Films*. 2005;474:119-126.
9. Can XT, Bing Y, Jun H, et al. Structural and mechanical properties of CrNx Coatings deposited by medium frequency magnetron sputtering with and without ion source assistance. *J Nanomater*. 2011;2011:1-7. Article ID 534647
10. Oner C, Hazar H, Nursoy M. Surface properties of CrN coated engine cylinders. *Mater Des*. 2009;30:914-920.
11. Alexander R, Elisabeth RP, Federico S. CrN coatings deposited by magnetron sputtering: mechanical and tribological properties. *Dyna*. 2015;82:147.
12. Choi HS, Han DH, Hong WH, et al. Titanium, chromium, nitride coatings for bipolar plate of polymer electrolyte membrane fuel cell. *J Power Sources*. 2009;189:966-971.
13. Jung DH, Park HS, Na HD, et al. Mechanical properties of (Ti, Cr)N coatings deposited by inductively coupled plasma assisted direct current magnetron sputtering. *Surf Coat Technol*. 2003;169–170:424-427.
14. Alexander R, Juan MG, Johans S, et al. Tribology of ZrN, CrN and TiAlN thin films deposited by reactive magnetron sputtering. *Dyna*. 2013;80:95-100.
15. Zhang GA, Yan PX, Wang P, et al. Influence of nitrogen content on the structural, electrical and mechanical properties of CrNx thin films. *Mater Sci Eng, A*. 2007;460–461:301-305.
16. Gregor M, Grown DR. *Optimization and Characterization of Reactively Sputtered Zirconium Nitride Thin Film for III-V Buffer Layer Applications*. Raleigh, NC: North Carolina State University; 2002.
17. Fellah M, Aissani L. Effect of milling time on sliding friction and wear behavior of hot isostatically pressed titanium alloys Ti-6Al-4X (X=V, Nb or Fe) for biomedical applications. ASME. *J Tribol*. 2017. https://doi.org/10.1115/1.4038103.
18. Feng X, Zhou H, Wan Z, et al. Effect of Ti content on structure and mechanical properties of Cr–Ti–N films. *Surf Eng*. 2017;33:619-625.
19. Liu Y, Zhao Q. Study of electroless Ni–Cu–P coatings and their anti-corrosion properties. *Appl Surf Sci*. 2004;228:57-62.
20. Kim GS, Kim BS, Lee SY, et al. Structure and mechanical properties of Cr–Zr–N films synthesized by closed field unbalanced magnetron sputtering with vertical magnetron sources. *Surf Coat Technol*. 2005;200:1669-1675.
21. Qian-Gang F, Li H-J, Xiao-Hong S, et al. Silicon carbide coating to protect carbon/carbon composites against oxidation. *Scripta Mater*. 2005;52:923-927.
22. Fellah M, Aissani L, Abdul Samad M, et al. Effect of replacing vanadium by niobium and iron on the tribological behavior of hiped titanium alloys. *Acta Metall Sin (Engl Lett)*. 2017;30:1089-1099.
23. Aouadi SM, Maeruf T, Twesten RD, et al. Physical and mechanical properties of chromium zirconium nitride thin films. *Surf Coat Technol*. 2006;200:3411-3417.
24. Mehran QM, Bushroa AR, Fazal MA. Evaluation of CrAlN multilayered coatings deposited by PVD magnetron sputtering. *Surf Eng*. 2015;29–19:2076-2089.
25. Shah HN, Jayaganthan R, Kaur D. Effect of sputtering pressure and temperature on DC magnetron sputtered CrN films. *Surf Eng*. 2010;26–8:629-637.
26. Chantharangsi C, Denchitcharoen S, Chaiyakun S. Structure and Surface Morphology of Cr-Zr-N Thin Films Deposited by Reactive DC Magnetron Sputtering. *Procedia Eng*. 2012;32:868-874.
27. Twu MJ, Hu CC, Liu DW, et al. Effects of TiN, CrN and TiAlN coatings using reactive sputtering on the fatigue behaviour of AA 2024 and medium carbon steel specimens. *J Exp Nanosci*. 2016;11–7:581-592.
28. Aissani L, Fellah M, Abdul Samad M, et al. Structural and mechanical properties of Cr-Zr-N coatings with different Zr content. *Surf Eng*, 2017;1-9. DOI.10.1080/02670844.2017.1338378.
29. Fellah M, Aissani L, Corinne N, et al. Characterization of R.F magnetron sputtered Cr-N, Cr-Zr-N and Zr-N coatings. *Trans IMF*. 2017;95:261-268.
30. Aissani L, Nouveau C, Walock M, et al. Influence of vanadium on structure, mechanical and tribological properties of CrN coatings. *Surf Eng*. 2015;31–10:779.
31. Fellah M, Labaïz M, Assala O, et al. Friction and wear behavior of Ti-6Al-7Nb biomaterial alloy. *J Biomater Nanobiotechno*. 2013;4:374.

32. Hones P, Sanjines R, Lvey F. Characterization of sputter-deposited chromium nitride thin films for hard coatings. *Surf Coat Technol*. 1997;91–95:398-402.
33. Oh UC, Je JH, Lee JY. Change of the critical thickness in the preferred orientation of TiN Films. *Mater Res*. 1995;10:634-639.
34. Fellah M. Sliding friction and wear performance of the nano-bioceramic α-Al_2O_3 prepared by high energy milling. Proceedings of the 14th International Conference on Tribology -SERBIA-TRIB'15, published by Serbian Tribology Society, Kragujevac. Edited by A.Vencl (13-15Mai 2015) 485-498 http://tribolab.mas.bg.ac.rs/proceedings.html
35. Conde A, Cristóbal AB, Fuentes G, et al. Surface analysis of electrochemically stripped CrN coatings. *Surf Coat Technol*. 2006;201:3588-3595.
36. Barshilia HC, Selvakumar N, Deepthi B, et al. A comparative study of reactive direct current magnetron sputtered CrAlN and CrN coatings. *Surf Coat Technol*. 2006;201:2193-2201.
37. Stypula B, Stoch J. The characterization of passive films on chromium electrodes by XPS. *Corros Sci*. 1994;36:2159-2167.
38. Lin J, Moore JJ, Moerbe WC, et al. Structure and properties of selected (CrAlN, TiCC, CrBN) nanostructured tribological coatings. *Int J Refract Metal Hard Mater*. 2010;28–1:2-14.
39. Re MD, Gouttebaron R, Dauchot JP, et al. Study of ZrN layers deposited by reactive magnetron sputtering. *Surf Coat Technol*. 2003;174–175:240-245.
40. Tański T, Lukaszkowicz K. Structure and properties of PVD coatings deposited on aluminum alloys. *Surf Eng*. 2012;28:598-604.
41. Mahieu S, Ghekiere P, Depla D, et al. Biaxial alignment in sputter deposited thin films. *Thin Solid Films*. 2006;515:1229-1249.
42. Bhatti J, Fazal MA, Khan AF, et al. Investigation of the mechanical properties of electrodeposited nickel and magnetron sputtered chromium nitride coatings deposited on mild steel substrate. *J Adhes Sci Technol*. 2016;30:2224-2235.
43. Yeung WY, Dub SN, Wuhrer R. A nanoindentation study of magnetron Co-sputtered nanocrystalline ternary nitride coatings. *Sci Sinter*. 2006;38:211-221.
44. Lamni R, Sanjinés R, Parlinska-Wojtan M, et al. Microstructure and nanohardness properties of Zr-Al-N and Zr-Cr-N thin films. *J Vac Sci Technol, A*. 2005;23:593-598.
45. Khlifi K, Ben CA. Investigation of adhesion of PVD coatings using various approaches. *Surf Eng*. 2013;29:555-560.
46. Purandare YP, Ehiasarian AP, Santana A, et al. ZrN coatings deposited by high power impulse magnetron sputtering and cathodic arc techniques. *J Vac Sci Technol, A*. 2014;32:031507.
47. Fellah M, Labaïz M, Assala O, et al. Tribological behavior of Ti-6Al-4V and Ti-6Al-7Nb Alloys for Total Hip Prosthesis. *Adv Tribol*. 2014;7:13pages.
48. Chen C-S, Liu C-P, Tsao C-Y. Study of mechanical properties of PVD ZrN films, deposited under positive and negative substrate bias conditions. *Scripta Mater*. 2004;51:715-719.
49. Zhang JJ, Wang MX, Yang J, et al. Enhancing mechanical and tribological performance of multilayered CrN/ZrN coatings. *Surf Coat Technol*. 2007;201:5186-5189.
50. Pakala M, Lin RY. Reactive sputter deposition of chromium nitride coatings. *Surf Coating Technol*. 1996;81:233-239.
51. Kim DH, Zhang TF, Shin JH, et al. Microstructure and mechanical properties of Cr–Ni–N coatings deposited by HiPIMS. *Surf Eng*. 2016;32:4314-4320.
52. Davies KE, Gan BK, Kenzie M, et al. Correlation between stress and hardness in pulsed cathodic arc deposited titanium/vanadium nitride alloys. *J Phys: Condens Matter*. 2004;16:7947-7954.
53. Tung H-M, Huang J-H, Tsai D-G, et al. Hardness and residual stress in nanocrystalline ZrN films: effect of bias voltage and heat treatment. *Mater Sci Eng, A*. 2009;500:104-108.
54. Fellah M, Labaïz M, Assala O, et al. Tribological behavior of AISI 316L stainless steel for biomedical applications. *Tribol-Mater, Surf Interfaces*. 2013;7:135-149.
55. Vera-Cárdenas EE, Vite-Torres M, Lewis R. Surface and sliding wear behaviour of different coatings and steels. *Ingeniería Investigación y Tecnología*. 2012;XIII:85-96
56. Vera EE, Vite M, Vite J, et al. Comparative Analysis of the Experimental Results of Wear by Rolling Contact Fatigue (rcf) of Steel AISI 4140 Base and with Superfi cial Covering of Nitriding, Hard Chromium and TiN, Nordtrib Tampere, Finland (2008)-116-31
57. Fellah M, Labaïz M, Assala O, et al. *Comparative Study on Tribiological Behavior of Ti-6Al-7Nb and SS AISI 316L Alloys, for Total hip Prothesis*. Hoboken, NJ: John Wiley & Sons, Inc.USA. The Minerals, Metals & Materials Society (TMS); 2014:237: 237-246.
58. Fellah M, Labaïz M, Assala O, et al. Tribological behavior of biomaterial for total hip prosthesis. *Matériaux & Techniques*. 2014;102:601.
59. Fellah M, Labaïz M, Assala O, et al. Tribological behavior of biomaterials for total hip prosthesis. *Trends Biomater Artif Organs*. 2015;29:22-30.
60. Fellah M, Labaïz M, Assala O. *Tribological Behavior of Friction Couple: metal/Ceramic (Used for Head of Total Hip Replacement)"*. Hoboken, NJ: John Wiley & Sons, Inc., USA. Advances in Bioceramics and Porous Ceramics VI; 2013:34 45-57.
61. Hah SR, Fischer TE, Gruffel P, et al. Effect of grain boundary dopants and mean grain size on tribomechanical behavior of highly purified alpha – alumina in the mildregime. *Wear*. 1995;181–183:165-177.
62. Fellah M, Abdul Samad M, Labaiz M, Assala O, Iost A. Sliding friction and wear performance of the nano-bioceramic α-Al_2O_3 prepared by high energy milling. *Tribol Int*. 2015;91:151-159.

How to cite this article: Fellah M, Aissani L, Abdul Samad M, et al. Effect of Zr content on friction and wear behavior of Cr-Zr-N coating system. *Int J Appl Ceram Technol*. 2018;15:701-715. https://doi.org/10.1111/ijac.12833